FACTA UNIVERSITATIS
Series: **Mechanical Engineering** Vol. 22, Nº 2, 2024, pp. 165 - 186
https://doi.org/10.22190/FUME220523045N

Original scientific paper

MAXIMIZATION OF WEAR RATES THROUGH EFFECTIVE CONFIGURATION OF STANDOFF DISTANCE AND HYDRAULIC PARAMETERS IN ULTRASONIC PULSATING WATERJET

Akash Nag[1], Amit Rai Dixit[2], Jana Petrů[1], Petra Váňová[3], Kateřina Konečná[3], Sergej Hloch[1,4]

[1]Technical University of Ostrava, Faculty of Mechanical Engineering, Czech Republic
[2]Indian Institute of Technology (ISM) – Dhanbad, India
[3]Technical University of Ostrava, Faculty of Materials Science and Technology, Czech Republic
[4]Institute of Geonics of the Czech Academy of Sciences, Ostrava-Poruba, Czech Republic

ORCID iDs: Akash Nag https://orcid.org/0000-0003-0400-7739
Amit Rai Dixit https://orcid.org/0000-0001-6135-8098
Jana Petrů https://orcid.org/0000-0002-2378-5678
Petra Váňová https://orcid.org/0000-0002-0607-1278
Kateřina Konečná https://orcid.org/0000-0002-9633-0164
Sergej Hloch https://orcid.org/0000-0003-4066-0620

Abstract. *A pulsating waterjet is a technological modification of a conventional waterjet that utilizes ultrasonic vibrations to generate a modulated jet, resulting in repetitive fatigue loading of the material. The erosion efficiency of the ultrasonic pulsating waterjet is majorly determined by the hydraulic factors and its interaction with standoff distance. However, the dependency of the wear rates on different hydraulic factors and formulation of an implicit prediction model for determining effective standoff distance is still not present to date. Therefore, in this study, the combined dependency of the supply pressure (20-40 MPa), nozzle diameter (0.3-1.0 mm), and standoff distance (1-121 mm) on wear rates of AW-6060 aluminum alloy are studied. Statistical analysis is used to determine the statistically significant factors and formulate regression equations to determine output responses within the experimental domain. The surface topography and sub-surface microhardness of the eroded grooves were studied. The results show that both the disintegration depth and the material removal increase with an increase in the nozzle diameter and supply pressure. However, the dependency of the output responses on nozzle diameter is statistically more evident than supply pressure and two-way interactions. Cross-sectional images of the grooves showed typical hydrodynamic erosion characteristics in erosion cavities, subsurface voids, and material upheaving. The results of microhardness analysis showed an approximately 15-20% increase in hardness values compared to the untreated samples.*

Key words: *Pulsating waterjet, Disintegration depth, Volume removal, ANOVA, Microhardness*

Received: May 23, 2022 / Accepted November 30, 2022
Corresponding author: Amit Rai Dixit
Indian Institute of Technology (ISM) – Dhanbad, 826001, India
E-mail: amitraidixit@iitism.ac.in

1. INTRODUCTION

Waterjet technology and its technological modifications have historically been put into practice depending on the current level of knowledge and technical possibilities [1]. The aim of waterjet technology is to take advantage of its associated benefits, such as the cold and selective disintegration method, based on the mechanical properties of the material [2,3]. However, the broader use of this technology is limited due to a lack of high-efficiency abrasives [4], the operational issues of high-pressure pumps, and related maintenance of the components making it still not competitive with conventionally existing methods [5]. Therefore, extensive research is being carried out in this sector to significantly improve the performance of waterjet technologies. It has been observed that a maximum erosion rate is achieved during the initial phase of the jet impact with the material surface [6]. This is attributed to the fact that during the initial phase, impact pressure given by Eq. (1), generated by the jet is induced into the material, followed by stagnation pressure given by Eq. (2), after a specific period. The magnitude of impact pressure is multiple times higher than the stagnation [7]. However, this impact pressure acts for an infinitesimal period. Therefore, various ways to transform the continuous jet into a series of drops are being investigated extensively.

$$p_i = \frac{p_l v_l c_l}{1+\frac{p_l c_l}{p_s c_s}} \tag{1}$$

$$p_s = \frac{1}{2}\rho_l v_l^2 \tag{2}$$

A pulsating waterjet induces periodic loading into the material due to accelerated changes in impact and stagnation pressures decreasing the time interval for the mechanical relaxation of the material. These alternating pressures induce stress waves inside the material with the speed of sound [8]. The reflected wave also interacts and affects the induced wave and makes a local hotspot of constructive and destructive interference of stress waves. These hotspots help in propagating cracks on the surface or inside the material and cause intense fatigue failure, resulting in material erosion [9]. At the point of impact of the jet with the material, jet velocity instantly reduces to zero, leading to conversion of the kinetic energy into deformation energy, which further leads to the formation of the water shock or water hammer phenomenon. The pressure induced in the material is known as impact pressure [10]. This impact pressure is induced for a short period, after which the stagnation pressure starts to act on the material [11]. However, neither the impact pressure nor the stagnation pressure depends on the size of the droplet. Only the duration for which the impact pressure is applied depends upon the size of the droplet.

Several methods for achieving a discontinuity from a continuous waterjet have been investigated and are still being researched [12]. The natural breakup of the jet is observed in cases where the water stream exiting from the nozzle is acted upon by cohesive and disruptive forces leading to perturbations and oscillations in the jet. These oscillations are intensified under favorable flow conditions and break the continuous flow into drops. Surface tension was considered the main factor for the jet's natural breaking up, which restricted it to small modulation amplitudes and was observed for low-speed jets [13]. Therefore, the inertial method is used for high-speed jets with a high Reynolds number, modulation amplitude, and frequency, leading to bunching and forced breakup of the jet into a series of water droplets. In a forced breakup jet, the instability of the jet is due to the

finite magnitude of the initiating amplitude. The jet exits the nozzle as a continuous jet with unsteady cyclical modulated velocity, resulting in slow and fast bunches of the jet flowing together. Eventually, the faster section overtakes the slower section in each cycle, resulting in the separation of the continuous stream into discrete bunches of water elements. The drop formation obtained from the inertial method using axial velocity modulation was analyzed and concluded that it differed from Rayleigh's theory. Another apparatus to generate flow modulation used a rotary disc upstream of the nozzle [14], which causes resistance in the flow and induces a periodical variation in the discharge rate. However, its bulky design and quick-wearing rotating components were not suitable for practical purposes. Another method for modulating jet generation is self-resonating nozzles (SRNs) [15] or Helmholtz resonators. In this method, the flow modulation is due to the sudden change in the geometry of the nozzle or the resonating chamber [16]. Various materials have been efficiently eroded or disintegrated using this approach to modulation. However, the system's performance is determined by the viscosity and temperature of the liquid, and modulation of the jet depends significantly on the nozzle design accuracy, limiting its utilization over a wider application area. Another method for modulating the jet is to induce ultrasonic vibration into the water stream using an ultrasonic generator. Apart from the ultrasonic generator, this assembly consists of an ultrasonic sonotrode in the form of a conical needle present near the nozzle exit and an electromechanical piezoelectric-based ultrasonic transducer [17]. The ultrasonic needle vibrates axially with the desired amplitude, restricting the course of water flow from the maximum to minimum value periodically. This results in the generation of oscillations downstream in the direction of the jet, focusing the energy at one point. However, with lower supply pressure (p = 10 MPa) and oscillation frequency (f = 15 kHz), the ultrasonic needle submerged in the liquid cavitates and reduces its efficiency. Additionally, at very high pressure (p > 100 MPa), the sonotrode oscillations are insignificant in generating discrete bunching of the waterjet, reducing its wear rates.

Recently, another assembly based on the induction of ultrasonic vibration into a continuous jet for generating a modulated jet was developed at the Institute of Geonics v.v.i. of CAS, Czech Republic [18]. This setup consists of an ultrasonic cylindrical sonotrode fitted with a piezoelectric transducer that oscillates inside a high-pressure acoustic chamber *lc* [mm] whose length can be varied as desired. The ultrasonic sonotrode interacts with the incoming pressurized water p [MPa] inside this chamber and induces pressure fluctuations [19]. These fluctuations in pressure amplify while flowing through the chamber due to their converging shape [20]. The length of the acoustic chamber l_c is varied to account for the liquid compressibility and tuning of the acoustic system. This effectively transfers the ultrasonic energy from the generator to the nozzle exit d [mm], where the pressure pulsations transform into velocity fluctuations [21]. These velocity fluctuations generate cyclic axial jet velocity v_w [m/s] at the exit generating clusters of varying velocity water elements in the air. After traveling a specific distance, known as the breakup length, the modulated jet splits into discrete clusters of water elements. The breakup length of the modulated jet depends significantly upon the mean velocity of the jet, velocity modulation ratio, and modulation frequency. These discrete bunches of water elements impact the material surface periodically and accelerate the wear [22].

The performance of the pulsating water jet (PWJ) depends on various technological parameters and their interactions, which can be categorized into ultrasonic factors, erosion factors, hydraulic factors, and target material properties. The response to variation of these parameters can be observed via the efficiency of the PWJ in terms of disintegration depth,

volume removal, micro-hardness, and surface integrity. Several researchers have conducted various experiments to understand the influence of these input parameters on the material erosion capability of the pulsating waterjet. However, it was observed that wear rates of PWJ majorly depended on the hydraulic factor and standoff distance. Hydraulic parameters comprise of supply pressure, hydraulic power, nozzle diameter, nozzle shape, and liquid density. Supply pressure determines the flow rate and hydraulic energy of the PWJ. An increase in the supply pressure generates a high-speed jet having higher kinetic energy. This increased kinetic energy leads to more significant erosion effects [23]. Supply pressure also determines the standoff distance range corresponding to visible disintegration. An increase in supply pressure shifts the entire erosion range to a higher standoff distance [24]. With the increase in supply pressure, the breakup length of the PWJ leads to the formation of a bunching phenomenon at a higher standoff distance [25]. The type of nozzle used in PWJ depends upon its application. A circular nozzle focuses the jet into a specific material area compared to the flat nozzle, which guides the jet over a wider area. However, it was concluded by Srivastava M. et. al. [26] that enhancement of mechanical properties is better when using circular nozzle than when using a flat nozzle due to the concentration of hydraulic energy during peening. Nozzle dimension determines the flow rate of the jet at constant pressure. With an increase in the nozzle diameter, the modulated jet's flow rate and hydraulic energy increase, increasing the disintegration depths [27]. The density of the liquid used plays an important role. A comparative study performed by Hloch S. et al. [28] showed that deeper and higher volume removal was calculated using 0.9% physiological saline compared to water during the disintegration of bone cement. This study also confirmed that PWJ with saline as a working fluid could extract bone cement. Standoff distance also plays a significant role in determining the erosion mechanism. Standoff distance divides the whole erosion region into five segments: incubation, acceleration, culmination, depletion, and termination for a constant flow rate. All these stages are formed depending upon the morphology of the water clusters formed after the nozzle exit. With the increase in the standoff distance, the disintegration depth increases up to a specific limit and decreases with a further increase in the standoff distance [29].

To summarize, state of the art, it was observed that the output response of the PWJ in the form of erosion rate majorly depends on the supply pressure, nozzle diameter, standoff distance, acoustic chamber, and excitation frequency. It can be implicitly defined by Eq. (3).

$$E = f(p, d, z, l_c, f) \tag{3}$$

Moreover, among these variables, l_c and z are dependent variables and depend on p, d, and f, which are independent. The nature of the dependency of l_c on p, d, and f values have been discussed in a previous study [30]. However, the dependency of z on p and d values is still missing in the literature. Additionally, there is no implicit prediction model to predict the effective range of z for given p and d values. Moreover, in the previous studies, a single hydraulic parameter, i.e., either p or d, was used to predict the optimal standoff distance and its limits corresponding to material erosion. However, it could not estimate the z value when both p and d varied simultaneously, i.e., no relationship of z in terms of hydraulic power was given.

2. Problem Statement

Therefore, in this study, the simultaneous effect of nozzle diameter (d = 0.3 to 1.0 mm), supply pressure (p = 20, 30 and 40 MPa), and standoff distance (z = 1 to 121 mm) on disintegration depth (h), volume removal, and the microhardness of aluminum alloy were studied. Statistical methods were used to determine input factors' dependency and interactions on output responses within the selected experimental domain. Analytical equations were formulated to predict the effective standoff distance range and its optimal level for disintegration using supply pressure, nozzle diameter, and hydraulic power as variables. The micro-hardness and microstructural analysis of the disintegrated grooves was also carried out to understand the interaction of PWJ with the material.

3. Materials and Methods

The aluminum alloy AW-6060 was used to determine the optimum erosion capability of PWJ based on the variation of nozzle diameters, supply pressure, excitation frequency, and standoff distance. Aluminum alloy was selected as the workpiece material due to the advantage of being able to observe the eroded grooves generated by the PWJ, which were easily attributed to its ductile nature. The chemical composition and mechanical properties of the aluminium alloy AW-6060 used for the experiments are shown in Table.1. The sample used for the experiments was in plates of length 500 mm, width 100 mm, and thickness 5 mm. The microstructure of the sample used is shown in Fig. 1. This micrograph shows the cross-sectional plane of the sample perpendicular to the direction of the PWJ trajectory. The effect of rolling during the fabrication of the sample resulting in deformed grains, can be observed on both sides of the sample as compared to the middle section of the sample.

Table 1 Chemical and mechanical properties of the Aluminium alloy.

Chemical composition								
Al	Si	Mg	Fe	Mn	Ti	Zn	Cr	Cu
98.85	0.44	0.44	0.2	0.03	0.015	0.01	0.004	0.0071
Mechanical composition								
R_m [MPa]			$R_{p0.2}$ [MPa]		A [%]		Hardness [HB]	
218			185		12.56		79	

The sample plates were attached to the catcher tank using jigs and fixtures to avoid movement during the tests. A Hammelmann pump supplied the pressurized water with a maximum operating pressure of 160 MPa at a flow rate of 67 dm^3/min. In the current study, water supply pressure was kept at p = 20, 30, and 40 MPa for each nozzle diameter. Nozzle diameter variation was carried out using Hammelmann nozzle inserts. The diameter variation used ranged from d = 0.3 mm to 1.0 mm. In this study we used a 20 kHz prototype of the PWJ available at the Institute of Geonics of CAS for experimental investigation. This prototype uses a 20 kHz ultrasonic generator to excite the piezoelectric ceramics attached to the sonotrode, enabling them to vibrate at their spatial frequency. This vibration-induced pressurized water travels through an acoustic chamber to reach the nozzle exit. The acoustic chamber is designed to modulate or tune the system to the resonant frequency (f = 19 – 21 kHz), which is approximately ± 5% of the fundamental

frequency (20 kHz), depending upon the physical conditions of the flow. This frequency modulation can be achieved by changing the length of the acoustic chamber. A detailed procedure for selecting the optimal acoustic chamber length for various combinations of supply pressure and diameter can be found in previous work [30]. Therefore, all the experimental runs were carried out in the present study with optimal acoustic chamber length for all flow combinations.

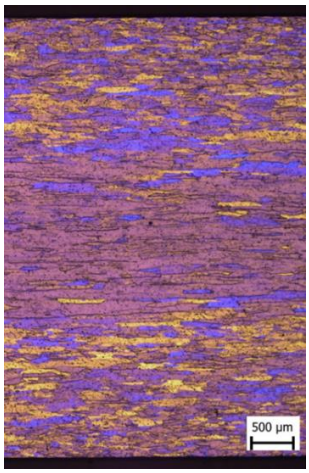

Fig. 1 Microstructure of the whole cross-section of the aluminum alloy AW-6060 sample

The standoff distance of the nozzle head from the sample was varied using a robotic arm which was also used to determine the trajectory and traverse speed (v = 5 mm/s) of the jet over the sample. A step trajectory with minimum step height z = 1 mm was selected for every experimental run with an increment of 2 mm in the vertical direction and 15 mm in the horizontal direction between consecutive steps. The maximum step height, z = 121 mm, was determined when no visible disintegration trace was observed using p = 40 MPa and d = 1 mm, which was carried out as a pilot study. A schematic representation of the experimental setup is shown in Fig. 2, and the experimental runs were carried out according to the parameters shown in Table 2.

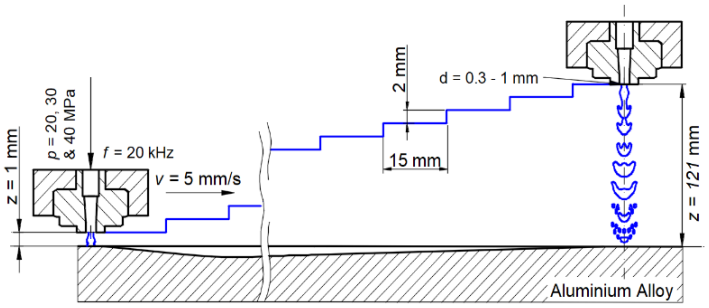

Fig. 2 Schematic representation of the experimental setup

Table 2 Experimental conditions

Run	Frequency [kHz]	Nozzle diameter [mm]	Supply pressure [MPa]	Acoustic chamber length [mm]	Flow rate [dm^3/min]	Hydraulic power [W]	Standoff distance [mm]
1	20	0.3	20	16	0.46	152.83	1 – 121
2			30	18	0.56	280.77	
3			40	19	0.65	432.28	
4		0.4	20	17	0.82	271.71	
5			30	19	1.00	499.15	
6			40	20	1.15	768.50	
7		0.5	20	18	1.27	424.54	
8			30	19	1.56	779.93	
9			40	20	1.80	1200.78	
10		0.6	20	20	1.83	611.34	
11			30	20	2.25	1123.10	
12			40	21	2.59	1729.12	
13		0.7	20	21	2.50	832.10	
14			30	21	3.06	1528.66	
15			40	22	3.53	2353.53	
16		0.8	20	21	3.26	1086.82	
17			30	22	3.99	1996.62	
18			40	22	4.61	3074.00	
19		0.9	20	21	4.13	1375.51	
20			30	22	5.05	2526.97	
21			40	22	5.84	3890.53	
22		1.0	20	21	5.09	1698.16	
23			30	22	6.24	3119.72	
24			40	22	7.20	4803.12	

*Discharge coefficient Cd = 0.9 for Hammelmann nozzle insert.

All 24 erosion grooves generated on the aluminum sample by combining the input parameters mentioned in Table 1 were scanned using a non-contact-type profilometer. The scanned data were analyzed using SPIP software to extract the groove information such as disintegration depth and volume removal for each groove generated by the PWJ. Specific samples produced by the PWJ using the extreme level of technological parameters, i.e., p = 20 and 30 MPa with d = 0.3 and 1.0 mm, were selected for detailed investigations. The cross-sectional topography of the generated grooves was studied using an Olympus IX70 light microscope. The cross-section of the sample's surface was polished and etched to observe the microstructural orientation of the material before and after the PWJ treatment. The morphology of the disintegrated groove was studied using a JEOL 6490LV scanning electron microscope (SEM) operating in secondary electron mode (SE). The overview micrographs were captured at a magnification of 13X, and the magnified images showing erosion characteristics were captured at 100X magnification. A microhardness study was also carried out on selected samples to observe the variation in the subsurface strengthening with different technological settings. The measurements were performed on a DuraScan G5 microhardness tester following the ČSN EN ISO 6507-1 standard for metallic samples. Indents were made with a load of 0.1 N, which was applied for 10 seconds on the cross-sectional plane of the sample perpendicular to the erosion direction. The indents were formed below the disintegrated groove at an equidistance of 60 μm between two consecutive indents up to a 2 mm depth from the starting point.

4. Results and Discussion

4.1. Effect on Disintegration Depth

Fig. 3 shows the variation in the disintegration depth with increasing standoff distance, supply pressure, and nozzle diameter. Each graph corresponds to a specific nozzle diameter kept constant, and the influence of supply pressure and standoff distance is observed. It is observed that the trend of the disintegration depth remains the same with increasing standoff distance for every combination of nozzle diameter and supply pressure. The erosion starts at a certain standoff distance (z_{vll}) and reaches a maximum value for a certain standoff distance (z_{opt}). A further increase in the standoff distance decreases the erosion capability, reduces the disintegration depth, and finally shows no visible erosion after a specific limit (z_{vul}). These lower and upper vertical limits of the standoff distance corresponding to measurable erosion range largely depend on the nozzle diameter and the supply pressure of the PWJ. The pulsating jet transforms into discrete bunches of water elements after covering a distance known as the breakup length [31]. This breakup length for a modulated jet depends significantly on the mean velocity of the jet, velocity modulation, and modulation frequency. However, it does not include the effect of the initial diameter of the jet. Additionally, the magnitudes of the induced impact and stagnation pressure in the material are independent of the nozzle diameter. However, the time duration for which impact pressure acts over the material surface depends upon the nozzle diameter before starting lateral jetting. Therefore, the erosive power increases either by increasing the nozzle diameter or the supply pressure when the nozzle diameter is constant. With the increase in the standoff distance, the pulsating jet that exits in continuous form starts to modulate and transform into discrete bunches of water elements. The phase from the exit until the breaking up of the jet shows no erosion or minimum erosion and is termed an incubation phase. Internal microstructural changes can occur in this phase, but no visible external erosion is observed on the material surface. When the standoff distance reaches a specific distance, where the distinct cluster formations start to generate, visible disintegration is observed. These repetitive impacts of water elements lead to the induction of impact pressure causing material disintegration. With the increase in the standoff distance, the disintegration depth also increases up to a specific limit. This phase is known as the acceleration phase. The phase at which the deepest disintegration is observed for each particular experimental condition corresponding to a certain standoff distance is the culmination phase. With a greater increase in the standoff distance, the aerodynamic effect starts affecting the modulation of the jet, and it starts flaring out, losing its effectiveness. Therefore, the disintegration depth values obtained decrease and are known as the depletion phase. With a further increase in the standoff distance of more than a specific limit, no erosion is observed due to the conversion of the PWJ into mono-dispersed droplets. This phase is known as the termination phase. All five phases for fixed technological parameters (p, d, v, l_c, and f) depend solely on the position of the sample material in relation to the nozzle exit. Therefore, proper setting up of standoff distance is required for the optimal utilization of the technology for material disintegration.

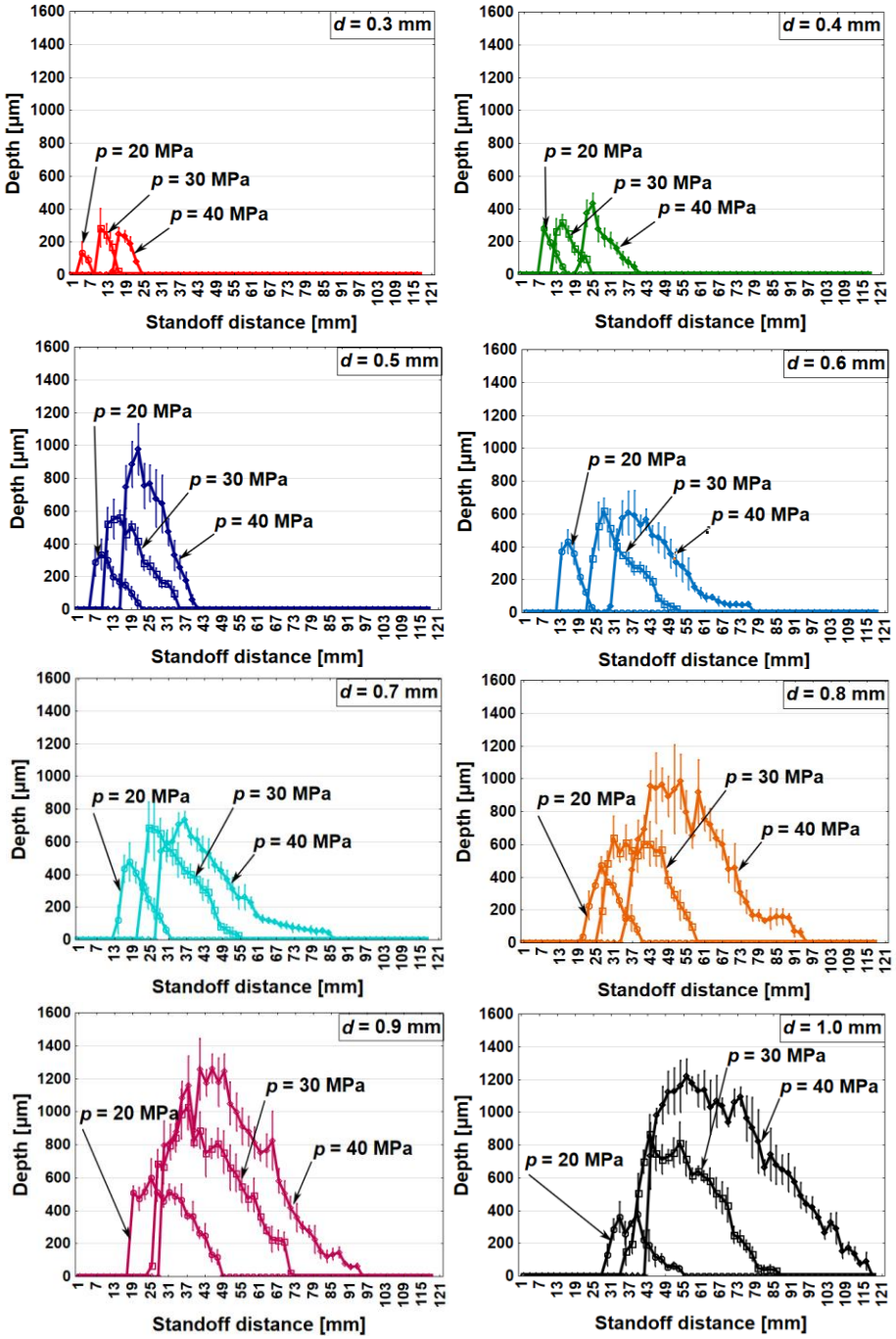

Fig. 3 Influence of nozzle diameter (d = 0.3 to 1 mm), supply pressure (p = 20, 30, and 40 MPa), and standoff distance (z = 1 to 121 mm) on disintegration depth (h)

Hydraulic power considers the effects of both pressure and nozzle diameter and, therefore, serves as a suitable parameter for predicting the erosion range in the standoff distance. Fig. 4 shows the variation in the standoff distance range corresponding to measured erosion with an increase in the hydraulic power for each combination of supply pressure and nozzle diameter. It can be observed that with the rise in hydraulic power, the lower vertical standoff distance (z_{vll}) marking the erosion initiation shifts to higher standoff distance values. Additionally, the erosion trace upper vertical limit (z_{vul}) increases, increasing the hydraulic power leading to the generation of deeper grooves for a larger range of vertical limits (z). The z_{vll}, z_{opt}, and z_{vul} of the standoff distance for a specific hydraulic power can be calculated using Eqs. (4), (5) and (6), respectively. The coefficients of determination, R-Sq (Adj), are 85.6%, 89.6%, and 95.2% for the lower, optimal, and upper limits of standoff distance, respectively. Therefore, the prediction of the range of z for which detectable erosion can be observed can be easily determined for any specific hydraulic power value corresponding to the combination of p and d values within the current experimental domain.

$$z_{vll} = 6.335 + 0.01274 * P_h - 0.000001 * P_h^2 \quad (4)$$

$$z_{opt} = 5.367 + 0.01843 * P_h - 0.000002 * P_h^2 \quad (5)$$

$$z_{vul} = 6.068 + 0.03584 * P_h - 0.000003 * P_h^2 \quad (6)$$

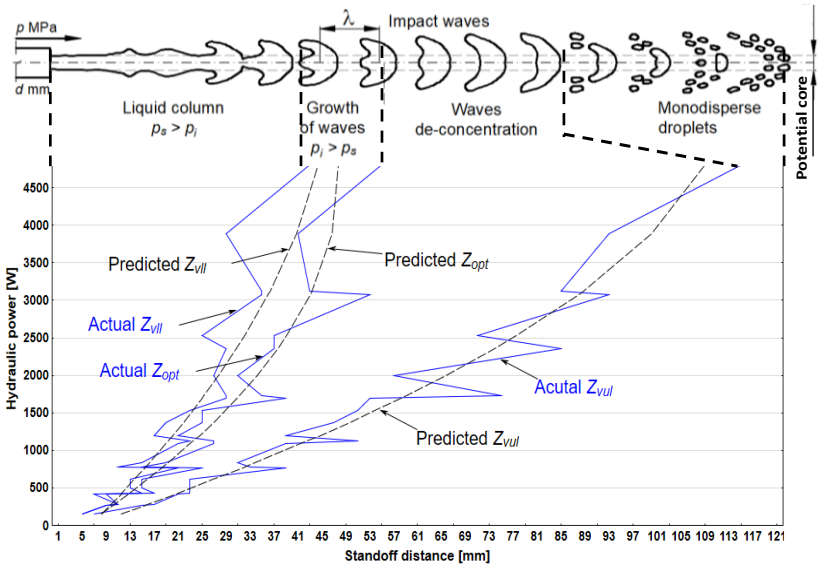

Fig. 4 Predicted and actual vertical lower, optimal and upper limit of standoff distance corresponding to visible erosion range for each combination of d = 0.3 to 1.0 mm and p = 20, 30, and 40 MPa.

4.2. Effect on Volume Removal

The volume of material removed during the interaction of PWJ with the aluminum surface for all combinations of the technological parameters is shown in Fig. 5.

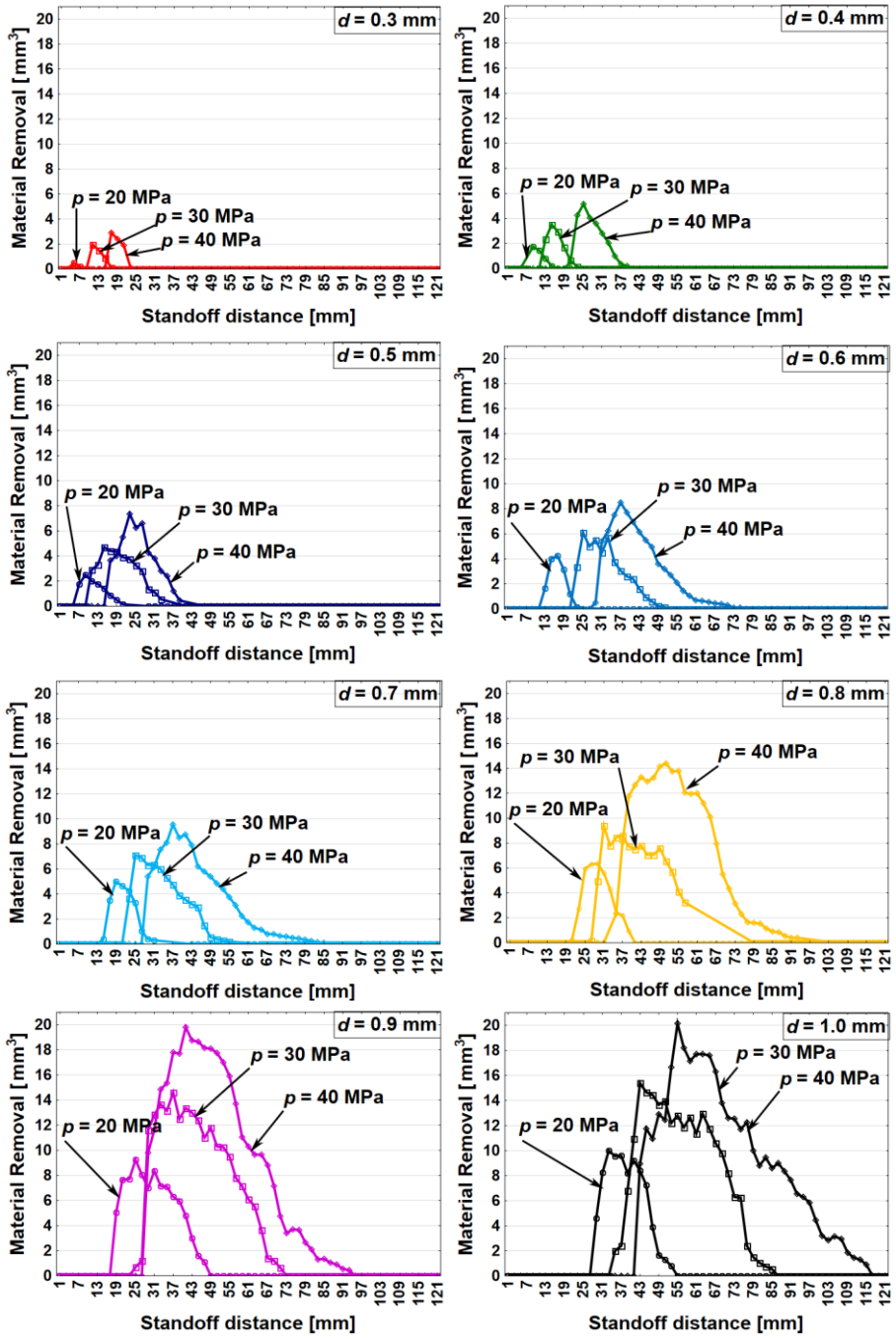

Fig. 5 Influence of nozzle diameter (d = 0.3 to 1 mm), supply pressure (p = 20, 30 and 40 MPa), and standoff distance (z = 1 to 121 mm) on material removal.

The disintegration length for each standoff distance was kept constant at 15 mm. Therefore, the volume of material removed depends significantly on the width and the depth of the eroded grooves. However, the trend of material removal is similar to the disintegration depth (Fig. 3) obtained for entire experimental runs. It can be observed that with the increase in both the supply pressure (p = 20 to 40 MPa) and nozzle diameter (d = 0.3 to 1.0 mm), material volume removal increases. The range of maximum volume removal varies from 0.48 to 20.17 mm^3 for p = 20 MPa, d = 0.3 mm to p = 40 MPa, and d = 1.0 mm, respectively. This increase in material volume removal is attributed to an increase in the flow rate from 0.46 to 7.20 dm^3/min and hydraulic power from 152 to 4803 W for p = 20 MPa, d = 0.3 mm to p = 40 MPa, and d = 1.0 mm, respectively.

4.3. Statistical Analysis

To observe the dependency of the disintegration depth achieved on the technological parameters, i.e., supply pressure and nozzle diameter, a full factorial design with three levels for supply pressure (p = 20, 30, and 40 MPa) along with eight levels for nozzle diameter (d = 0.3 to 1.0 mm) was used. Maximum values of both the responses (disintegration depth and material removal) at each combination of the experimental run were used for the analysis. An analysis of variance (ANOVA) [32,33] (Table 3) and a Pareto chart were used to identify the parameters or interaction of statistically significant ($P < 0.05$) parameters in determining the output responses, i.e., the disintegration depth and material volume removal.

Table 3 Analysis of variance for disintegration depth and material removal

Disintegration depth					
Source	DF	Contribution	F-Value	P-Value	VIF
Model	3	85.15%	38.22	0	
Linear	2	78.00%	52.52	0	
p	1	31.56%	42.49	0	1
d	1	46.45%	62.54	0	1
Two-Way Interactions	1	7.14%	9.62	0.006	
*p*d*	1	7.14%	9.62	0.006	1
Error	20	14.85%			
Total	23	100.00%			
Modal Summary: S = 128.483, R-sq = 85.15%, R-sq(adj) = 82.92%, R-sq(pred) = 77.53%					
Disintegration depth = 239 - 7.32 * *p* - 399 * *d* + 43.5 * *p* * *d*					
Material removal					
Source	DF	Contribution	F-Value	P-Value	VIF
Model	3	95.86%	154.47	0	
Linear	2	91.60%	221.40	0	
p	1	20.87%	100.88	0	1
d	1	70.73%	341.92	0	1
Two-Way Interactions	1	4.26%	20.61	0	
*p*d*	1	4.26%	20.61	0	1
Error	20	4.14%			
Total	23	100.00%			
Modal Summary: S = 1.19972, R-sq = 95.86%, R-sq(adj) = 95.24%, R-sq(pred) = 94.29%					
Material removal = -2.36 - 0.0850 * *p* + 1.94 * *d* + 0.594 * *p* * *d*					

The results show that the models for depth and volume are both statistically significant. For the disintegration depth model, linear and two-way interaction models contribute 78.00% and 7.14%. Nozzle diameter (46.45%) is the most statistically significant parameter for determining disintegration depth, followed by supply pressure (31.56%) and the interaction of both supply pressure and nozzle diameter (7.14%) for the selected experimental range domain. The ANOVA results also show that the presented statistical model can accurately predict 77.53% of the disintegration depth values within the experimental domain. For material removal, the linear model (91.60%) contributes significantly compared to the two-way interaction model (4.26%). Additionally, for material removal, nozzle diameter (70.73%) is the most influential parameter as compared to supply pressure (20.87%) and the interaction of supply pressure and nozzle diameter (4.26%). The predictability of the material removal values is nearly 94.29% with the presented statistical model within the selected experimental domain. Therefore, it can be concluded that variation in the nozzle diameter affects the responses, i.e., the depth and the material volume, significantly, followed by supply pressure within the selected experimental domain.

Pareto charts of effects for both disintegration depth and material volume were plotted to determine the magnitude and importance of the effects (Fig. 6). The bar corresponding to the effect that crosses the reference line (2.086 for depth and 2.09 for material removal) was considered to be statistically significant for the given output response. The Pareto chart agrees with the ANOVA results, i.e., for both the responses, nozzle diameter is the most influential parameter followed by supply pressure and then the interaction of both the nozzle diameter and the supply pressure. However, for material removal, the nozzle diameter is a significantly effective parameter for determining its value compared to any other parameters determining the disintegration depth.

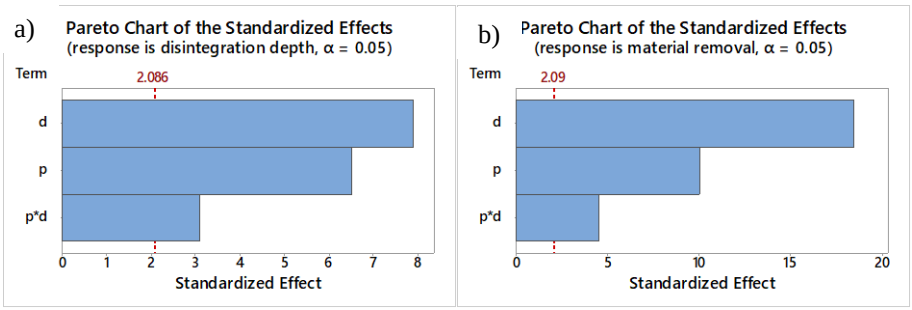

Fig. 6 Pareto chart of effects for a) disintegration depth and b) material removal

Fig. 7 shows the maximum disintegration depth response surface and material removal with supply pressure and nozzle diameter variation. These surface plots depict how the response trends change with a simultaneous change in input parameters. For a lower nozzle diameter (d = 0.3 mm), with an increase in supply pressure from p = 20 to 40 MPa, the differences in the maximum disintegration depth and material volume removal are observed to be 114 µm and 2.4175 mm^3, respectively, as compared to 840 µm and 10.1528 mm^3 for a larger nozzle diameter, d = 1.0 mm. This significant variation in response values, even keeping the same pressure range, is due to the variation in the flow rate and the hydraulic power for d = 0.3 mm (0.19 dm^3 and 279.45 W) compared to d = 1.0 mm (2.11

dm^3 and 3104.96 W). Therefore, the surface plot provides a better selection of input parameters according to the desired output response. It is recommended to use a larger nozzle diameter with lower pressure values for applications where deeper disintegration and higher material removal are required. However, for applications with a precise and limited area for extracting or disintegrating material, a smaller nozzle diameter with higher supply pressure can be used efficiently to achieve the desired results.

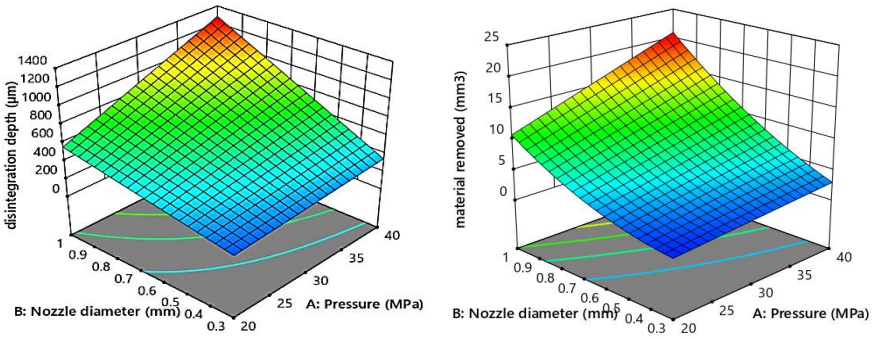

Fig. 7 Response surface plot of disintegration depth and material removal with nozzle diameter and supply pressure.

Statistical analysis can also determine the z_{vll}, z_{opt}, and z_{vul} for any combination of p and d within the selected experimental domain. This aids in the prediction of the effective range of z, where detectable erosion can be observed. The predictability values of z_{vll}, z_{opt}, and z_{vul} with the regression equations mentioned in Eqs. (7), (8) and (9) are calculated to be R-Sq (Pred) = 86.66%, 89.40%, and 96.07%, respectively.

$$z_{vll} = -19.11 + 0.625 * p + 32.86 * d \quad (7)$$

$$z_{opt} = -29.95 + 0.85 * p + 47.62 * d \quad (8)$$

$$z_{vul} = -11.1 - 0.06 * p - 0.7 * d + 3.226 * p * d \quad (9)$$

4.4. Surface Topography

Fig. 8 represents the cross-sectional images of the disintegration groove generated at optimal standoff distance for extreme levels of both supply pressure and nozzle diameter selected in this study, i.e., p = 20 and 40 MPa and d = 0.3 mm and 1.0 mm. Fig 8a represents the erosion at the minimum flow rate, i.e., Q = 0.43 dm^3/min and 152.83 W hydraulic energy. A disintegration trace with a mean groove depth of h = 134 µm is obtained. Isolated voids formed due to micro-channeling in the sub-surface region of the impacted area are observed (Fig. 8b). These micro-channels originate from the groove cavity and propagate in different directions throughout the vicinity of the eroded groove [34]. A broader and deeper groove (h = 248 µm) is obtained with an increase in supply pressure from p = 20 to 40 MPa, keeping nozzle diameter the same, as d = 0.3 mm (Fig. 8c). An asymmetric erosion groove is formed, which can be attributed to the localized material properties during the interaction of the PWJ with the material surface. Material upheaving is observed at the boundary of the disintegrated groove (Fig. 8d). This material upheaving is significantly due

to the radial outflow of the impacted water stream known as lateral jetting. The shear stress generated pushes the material towards the erosion periphery resulting in curved material flow.

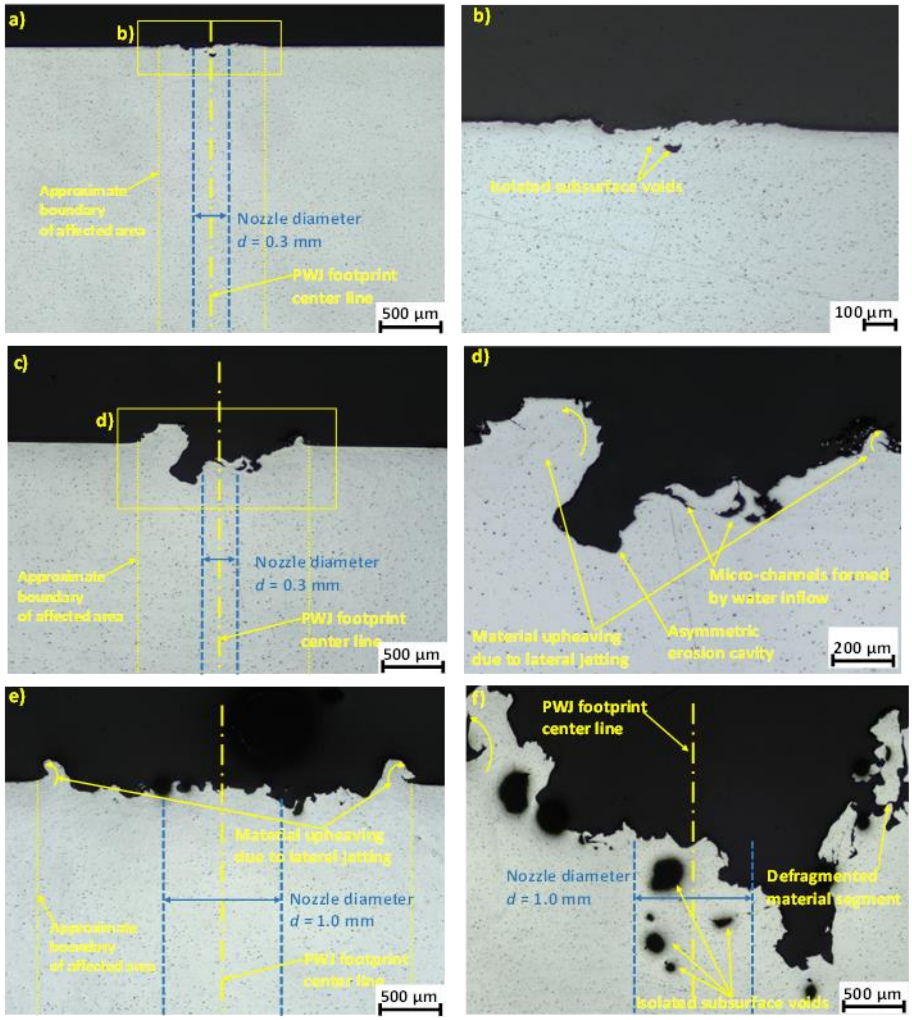

Fig. 8 Cross-sectional view of deepest disintegration trace generated at a) d = 0.3 mm, p = 20 MPa, b) magnified view of impacted region of Fig. a, c) d = 0.3 mm, p = 40 MPa, d) magnified view of impacted region of Fig. c, e) d = 1.0 mm, p = 20 MPa and f) d = 1.0 mm, p = 40 MPa.

With the increase in the nozzle diameter, from d = 0.3 mm to 1.0 mm, the disintegration groove volume increases. An erosion crater, isolated subsurface voids, and material upheaving are also shown in Fig. 8e. It can be observed that groove width significantly depends on the nozzle diameter. However, the depth of the groove is determined by the

supply pressure. From a volume removal point of view, selecting a larger nozzle diameter is more beneficial even with lower pressure levels. Statistical analysis resulted in the same observation. However, if a specific groove width or disintegration of the intricate area is required, a smaller nozzle diameter with more considerable supply pressure can be used. With a further increase in the supply pressure p = 40 MPa, a deeper erosion groove than p = 20 MPa is obtained. The disintegration trace is heavily eroded with an asymmetric groove profile (Fig. 8f). Eroded material fragments dislodged due to the jet impact, and lateral jetting, can be observed near the eroded groove wall. Isolated holes formed by the micro-jet streams penetrating the material and localized material interaction can be observed in the subsurface region around the disintegrated groove. These craters or voids can also be present in the parent material and act as stress concentration sites that promote or accelerate material failure under hydraulic impact [35].

4.5. Surface Morphology

Fig. 9 shows the micrographs of the disintegrated grooves of the selected sample produced using extreme parameter levels (p = 20 and 40 MPa, d = 0.3 and 1.0 mm). The material damage and erosion are largely caused by the induction of compressive stress during the PWJ impact, followed by shear stress due to the lateral flow of the jet. When they exceed the ultimate tensile limit of the aluminum alloy (215 MPa), the combined induced stresses result in material failure and removal. Fig. 9a shows the groove generated using d = 0.3 mm and p = 20 MPa at z = 5 mm. At these technological conditions, the average width and depth of the groove were measured as w = 940 µm and h = 164 µm, respectively. The compressed area due to the PWJ impact followed by water flowing away from the PWJ footprint center was observed in Fig. 9b. Cavity rims and entrances are generated due to the jet's repetitive impact, causing the aluminum alloy to undergo material damage. With the increase in the pressure, p = 40 MPa, a larger erosion groove is obtained, having an approximate width of w = 1400 µm and a mean depth of h = 248 µm (Fig. 9c). PWJ under these technological conditions possesses higher hydraulic energy (432 W), producing greater erosion damage. Dimple formation due to the interaction of PWJ with ductile material can be seen near the PWJ centerline. Moreover, sites acting as an opening for the water flow to penetrate deeper into the materials are also observed in Fig. 9d. Fig. 9e shows the disintegration trace produced by PWJ with d = 1.0 mm and p = 20 MPa at z = 33 mm. The hydraulic energy and flow rate of the PWJ at this parameter setting are P = 1698 W and Q = 5.09 dm^3/min. This results in higher impact pressure on the surface inducing larger compressive stress in the material. A wider disintegration groove, w = 3100 µm, with a mean depth, h = 379 µm, is obtained. Micro-cavities of varying dimensions are randomly generated through the disintegrating surface of the material (Fig. 9f). Fig. 9g represents the micrograph of the disintegrated area produced by PWJ with d = 1.0 mm and p = 40 MPa at z = 125 mm. Average disintegration width, w = 4700 µm, and depth, h = 1211 µm, were obtained during this experimental run. The image also shows the material upheaval caused by the lateral flow of the PWJ, generating an approximate boundary of the erosion groove. The bottom of the groove is heavily articulated with several cavity openings caused by material deformation. From a fractographic point of view, the image shows the area with different modes of material erosion. A section of the compressed material surface formed along the PWJ footprint centerline can be observed in Fig. 9.

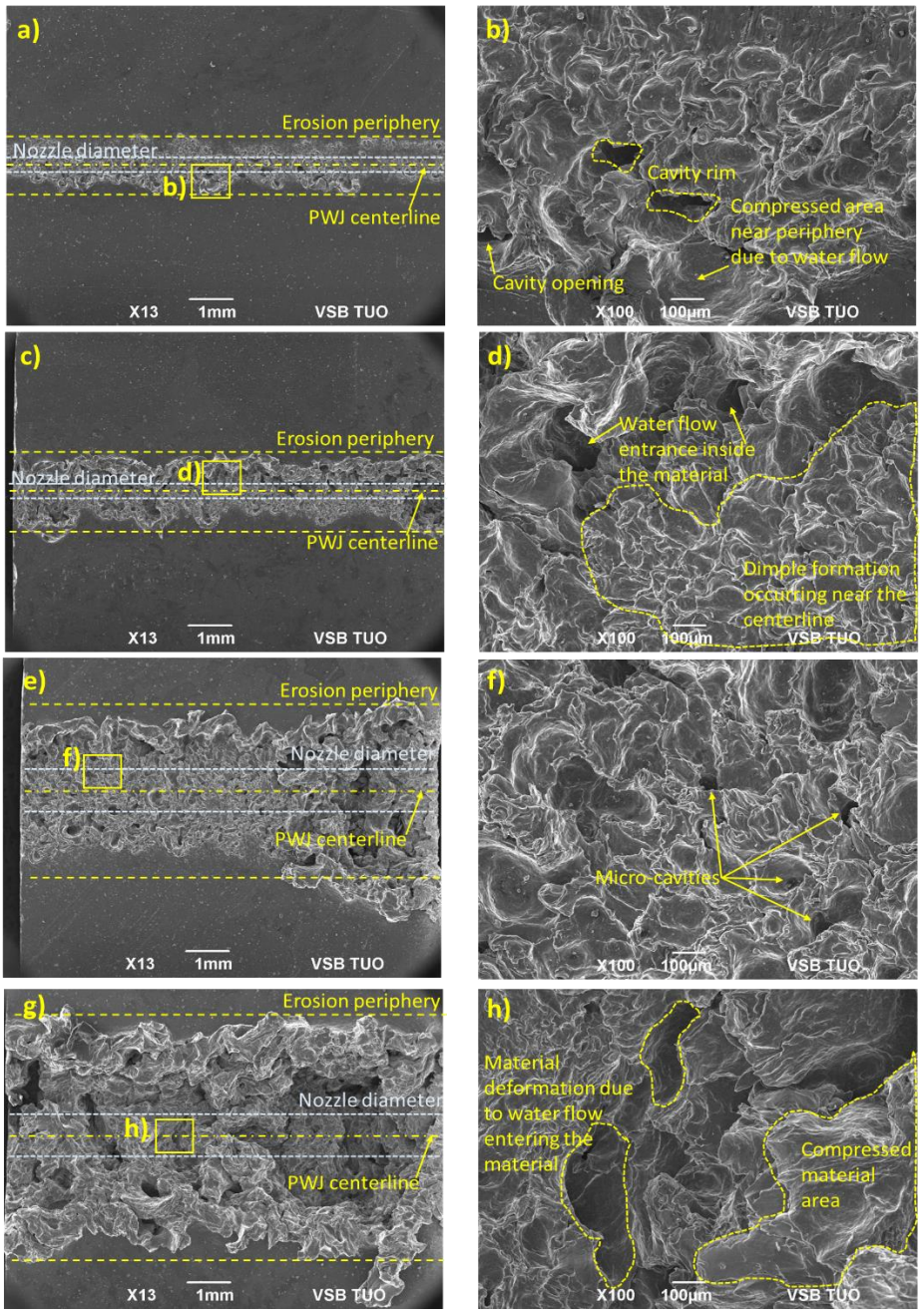

Fig. 9 SEM images of disintegrated samples generated by PWJ at different technological conditions a) d = 0.3 mm, p = 20 MPa, z = 5 mm, c) d = 0.3 mm, p = 40 MPa, z = 17 mm, e) d = 1.0 mm, p = 20 MPa, z = 33 mm and g) d = 1.0 mm, p = 40 MPa, z = 125 mm. The magnified images of the marked areas (b, d, f, and h) are also shown.

4.6. Microhardness

Microhardness analysis was performed to determine the change in the sub-surface hardness near the periphery of the eroded groove. The measurements were carried out with a load of 0.1 N starting below the disintegrated groove on the cross-sectional plane until a depth of 2 mm. The distance between two consecutive indents was kept at 60 µm. The sites for microhardness tests for all four samples are shown in Fig. 10.

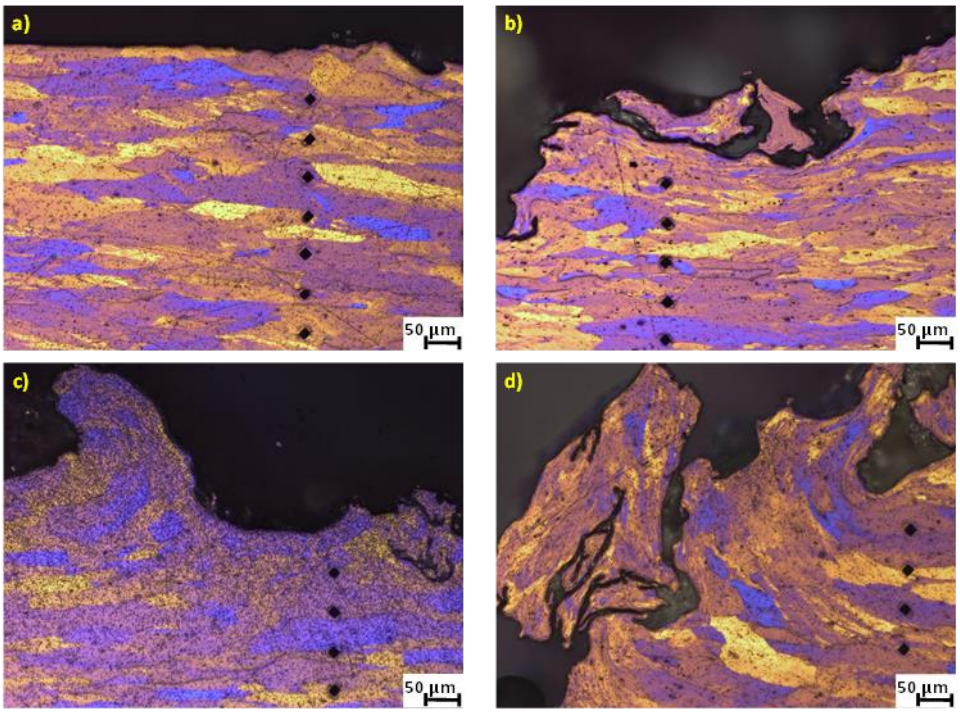

Fig. 10 Microhardness measurement sites on different samples eroded with different parameter conditions: a) d = 0.3 mm, p = 20 MPa, z = 5 mm, b) d = 0.3 mm, p = 40 MPa, z = 17 mm, c) d = 1.0 mm, p = 20 MPa, z = 33 mm, and d) d = 1.0 mm, p = 40 MPa, z = 125 mm.

Fig. 11 shows the variation in microhardness data with increasing depth from the bottom of the groove on the cross-sectional plane. It can be observed that an increase of 15 – 20 % is recorded for the eroded samples throughout the depth as compared to original samples in their received form. For PWJ, the impact pressure induced on the surface leads to plastic deformation in the form of increased dislocation density. This enhancement in dislocation density is attributed to grain refinement and the formation of slip lines near the impacted surface. The cyclical impact induces compressive stresses that propagate along the material cross-section leading to strengthening of the sub-surface in form of enhanced microhardness. However, the influence of the levels of the technological parameters (supply pressure, nozzle diameter, and standoff distance) on the subsurface strengthening determined by microhardness values is not visible. The subsurface hardening obtained at

d = 0.3 mm and p = 20 MPa is almost similar to that obtained at d = 1.0 mm and p = 40 MPa. However, the disintegration depth or material removal varies significantly for these technological levels. This non-significant difference in microhardness values can be associated with the small range (~25 MPa) (tensile strength R_m = 215 MPa and yield point $R_{p0.2}$ = 190 MPa) of the plastic zone for the AW-6060 aluminum alloy used in the current study. These properties of AW-6060 aluminum alloy create a small range for generating plastic deformation without affecting the tensile strength and lead to the material removal process at any technological level. Therefore, the surfaces exposed to PWJ are damaged and form disintegrated grooves at given technological levels. The variation in the microhardness of the unaffected material throughout the depth is also attributed to the distribution of the grain structure and its orientation. The microstructural distribution near the sample surfaces is randomly oriented and deformed in size compared to the grains present in the center of the sample due to the rolling action during the fabrication of the samples.

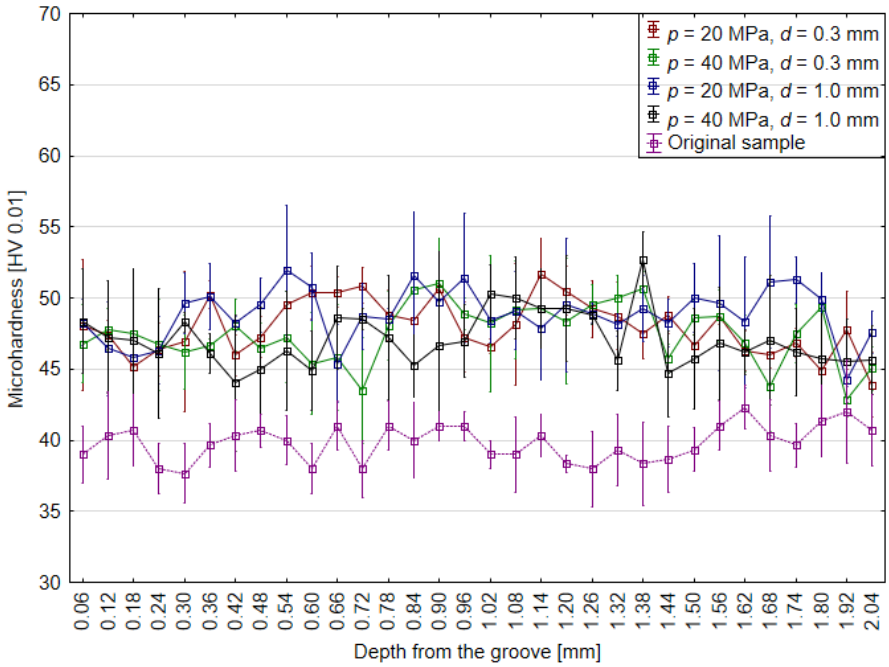

Fig. 11 Microhardness trend along the cross-sectional plane below the disintegrated groove formed under different technological conditions.

5. CONCLUSIONS

In this study we investigated the utilization of the water hammer effect produced by an ultrasonic pulsating waterjet for disintegration of materials. The appropriate setting of technological parameters is not only necessary to maximize the disintegration but also by merely changing the distribution of impacts, PWJ can be used for surface roughening and increasing fatigue life through peening. In this study, the nozzle diameter, supply pressure,

and standoff distance were selected to observe their effect on disintegration depth, volume removal, microhardness, and the surface morphology of the disintegrated material. Statistical analysis was used to determine the statistically significant input parameters for the output responses and to formulate statistical regression equations to predict effective range and optimal standoff distance. The major findings of the study are summarized as follows:

1) A simultaneous increase in supply pressure (p = 20, 30, and 40 MPa) and nozzle diameter (d = 0.3 – 1.0 mm) increases the disintegration depth and material removal values. Additionally, with a specific combination of p and d, the disintegration depth and material removal increase with the standoff distance up to a certain limit and then decrease with a further increase in the standoff distance.
2) Sharp increase in erosion compared to gradual decrease due to air drag was observed while increasing the z values (z = 1 to 121 mm) (Fig.5). This corresponds to smaller difference between the optimal standoff distance (z_{opt}) and vertical lower limit of standoff distance (z_{vll}) as compared to vertical upper limit of standoff distance (z_{vul}) and z_{opt} for all experimental conditions.
3) The hydraulic power of PWJ was observed as a suitable indicator to identify the effective limits of standoff distance. Eqns. 6, 7, and 8 showed that lower, optimal, and higher limits of the standoff distance could be easily predicted using hydraulic power as a variable.
4) Analysis of variance results showed that the dependence of disintegration depth and material removal is higher for nozzle diameter (46.45% and 70.73%) as compared to supply pressure (31.56% and 20.87%) and two-way interactions (7.14% and 4.26%). The regression equations formulated allow the prediction of the values of the output responses within the selected experimental domain.
5) Statistical regression equations were formulated to predict the effective range and optimal standoff distance using nozzle diameter and supply pressure values.
6) The cross-sectional topography of the selected samples shows the extent of the disintegration grooves inside the material and the upheaved material section formed at the periphery of the groove due to the lateral jetting.
7) SEM images captured the overall disintegration traces and detailed erosion characteristics such as the formation of crater openings and compressed and ductile erosion regions for the selected samples.
8) A microhardness study showed an increase of 15 – 20% in microhardness values after impact with the PWJ compared to the original state. However, no significant variation in the values was noticed due to a change in the parameter levels. This is attributed to the slight difference (~25 MPa) between the yield and ultimate tensile values of the AW-6060 aluminum alloy that was used.

The outcomes of this study would help to quickly tune the technology to resonance while also using it for practical purposes. A tuning methodology is proposed according to the implicit function for the determination of the optimal and effective range of standoff distance, which simplifies further research.

Acknowledgement: *This work was supported by financial support by the Czech Science Foundation, project GACR 19-00408S.*

REFERENCES

1. Perec, A., Radomska-Zalas, A., Fajdek-Bieda, A., 2022, *Experimental research into marble cutting by abrasive water jet*, Facta Universitatis-Series Mechanical Engineering, 20(1), pp. 145–156.
2. Natarajan, Y., Murugesan, P.K., Mohan, M., Khan, S.A.L.A., 2020, *Abrasive water jet machining process: A state of art of review*, Journal of Manufacturing Processes, 49, pp. 271–322.
3. Kumar, R., Chattopadhyaya, S., Dixit, A.R., Bora, B., Zelenak, M., Foldyna, J., Hloch, S., Hlavacek, P., Scucka, J., Klich, J., Sitek, L., Vilaca, P., 2017, *Surface integrity analysis of abrasive water jet-cut surfaces of friction stir welded joints*, International Journal of Advanced Manufacturing Technology, 88(5–8), pp. 1687–1701.
4. Perec, A., 2018, *Experimental research into alternative abrasive material for the abrasive water-jet cutting of titanium*, The International Journal of Advanced Manufacturing Technology, 97(1), pp. 1529–1540.
5. Vijay, M.M., Foldyna, J., Remisz, J., 2018, *Ultrasonic modulation of high-speed water jets*, in: Geomechanics 93, Routledge, pp. 327–332.
6. Fujisawa, N., Takano, S., Fujisawa, K., Yamagata, T., 2018, *Experiments on liquid droplet impingement erosion on a rough surface*, Wear, 398–399, pp. 158–164.
7. Kang, Y., Xie, F., Shi, H., Wu, N., Wang, Z., Wang, X., Hu, Y., Li, D., 2021, *Experimental investigation on the penetration characteristics of low-frequency impact of pulsed water jet*, Wear, 448–449, 204145.
8. Foldyna, J., Sitek, L., Ščučka, J., Martinec, P., Valíček, J., Páleníková, K., 2009, *Effects of pulsating water jet impact on aluminium surface*, Journal of Materials Processing Technology, 209(20), pp. 6174–6180.
9. Peng, J., Wong, L.N.Y., Teh, C.I., 2017, *Influence of grain size heterogeneity on strength and microcracking behavior of crystalline rocks*, Journal of Geophysical Research: Solid Earth, 122(2), pp. 1054–1073.
10. Nag, A., Hloch, S., Dixit, A.R., Pude, F., 2020, *Utilization of ultrasonically forced pulsating water jet decaying for bone cement removal*, The International Journal of Advanced Manufacturing Technology, 110(3–4), pp. 829–840.
11. Nag, A., Hvizdos, P., Dixit, A.R., Petrů, J., Hloch, S., 2021, *Influence of the frequency and flow rate of a pulsating water jet on the wear damage of tantalum*, Wear, 477, 203893.
12. Říha, Z., Zeleňák, M., Kruml, T., Poloprudský, J., 2021, *Comparison of the disintegration abilities of modulated and continuous water jets*, Wear, 478, 203891.
13. Blaisot, J.B., Adeline, S., 2003, *Instabilities on a free falling jet under an internal flow breakup mode regime*, International Journal of Multiphase Flow, 29(4), pp. 629–653.
14. Dehkhoda, S., Hood, M., 2013, *An experimental study of surface and sub-surface damage in pulsed water-jet breakage of rocks*, International Journal of Rock Mechanics and Mining Sciences, 63, pp. 138–147.
15. Zeleňák, M., Říha, Z., Jandačka, P., 2020, *Visualization and velocity analysis of a high-speed modulated water jet generated by a hydrodynamic nozzle*, Measurement, 159, 107753.
16. Gensheng, L., Zhonghou, S., Changshan, Z., Debin, Z., Hongbing, C., 2005, *Investigation and application of self-resonating cavitating water jet in petroleum engineering*, Petroleum Science and Technology, 23(1), pp. 1–15.
17. Amegadzie, M.Y., Moreau, E.D., Christensen, B., Donaldson, I.W., Tieu, A., Vijay, M.M., Plucknett, K.P., 2021, *Ultrasonic pulsed waterjet surface peening of an industrial aluminum-based metal matrix composite*, Surface and Coatings Technology, 426, 127795.
18. Foldyna, J., 2011,*Use of acoustic waves for pulsating water jet generation*, in: Acoustic Waves: From Microdevices to Helioseismology, IntechOpen, 14, pp. 323–342.
19. Foldyna, J., Sitek, L., Habán, V., 2006, *Acoustic wave propagation in high-pressure system*, Ultrasonics, 44, pp. e1457–e1460.
20. Pochylý, F., Habán, V., Foldyna, J., Sitek, L., 2007, *3D problem of pressure wave propagation in the tube with inconstant cross section*, in: Proceedings of the International Congress on Ultrasonics, Vienna, pp. 1–4.
21. Foldyna, J., Říha, Z., Sitek, L., Švehla, B., 2007, *Numerical simulation of transmission of acoustic waves in high-pressure system*, in: Proceedings of the International Congress on Ultrasonics, Vienna, pp. 1–4.
22. Hreha, P., Hloch, S., Magurovd, D., Valicek, J., Kozak, D., Harnicdrovd, M., Rakin, M., 2010, *Water jet technology used in medicine*, Tehnicki Vjesnik, 17(2), pp. 237–240.
23. Tripathi, R., Hloch, S., Chattopadhyaya, S., Klichová, D., Ščučka, J., Das, A.K., 2020, *Application of the pulsating and continous water jet for granite erosion*, International Journal of Rock Mechanics and Mining Sciences, 126, 104209.
24. Hloch, S., Srivastava, M., Nag, A., Muller, M., Hromasová, M., Svobodová, J., Kruml, T., Chlupová, A., 2020, *Effect of pressure of pulsating water jet moving along stair trajectory on erosion depth, surface morphology and microhardness*, Wear, 452-453, 203278.
25. Srivastava, M., Hloch, S., Gubeljak, N., Milkovic, M., Chattopadhyaya, S., Klich, J., 2019, *Surface integrity and residual stress analysis of pulsed water jet peened stainless steel surfaces*, Measurement, 143, pp. 81–92.

26. Srivastava, M., Hloch, S., Tripathi, R., Kozak, D., Chattopadhyaya, S., Dixit, A.R., Foldyna, J., Hvizdos, P., Fides, M., Adamcik, P., 2018, *Ultrasonically generated pulsed water jet peening of austenitic stainless-steel surfaces*, Journal of Manufacturing Processes, 32, pp. 455–468.
27. Nag, A., Hloch, S., Dixit, A.R., 2021, *On-Line Monitoring of In-Vitro Application of PWJ for Bone Cement Disintegration*, in: Advances in Manufacturing Engineering and Materials II, Lecture Notes in Mechanical Engineering, Springer, pp. 100–110.
28. Hloch, S., Nag, A., Pude, F., Foldyna, J., Zeleňák, M., 2019, *On-line measurement and monitoring of pulsating saline and water jet disintegration of bone cement with frequency 20 kHz*, Measurement, 147, 106828.
29. Hloch, S., Adamčík, P., Nag, A., Srivastava, M., Čuha, D., Müller, M., Hromasová, M., Klich, J., 2019, *Hydrodynamic ductile erosion of aluminium by a pulsed water jet moving in an inclined trajectory*, Wear, 428-429, pp. 178–192.
30. Nag, A., Stolárik, G., Svehla, B., Hloch, S., 2021, *Effect of Water Flow Rate on Operating Frequency and Power During Acoustic Chamber Tuning*, in: Advances in Manufacturing Engineering and Materials II, Lecture Notes in Mechanical Engineering, Springer, pp. 142–154.
31. Poloprudský, J., Nag, A., Kruml, T., Hloch, S., 2021, *Effects of liquid droplet volume and impact frequency on the integrity of Al alloy AW2014 exposed to subsonic speeds of pulsating water jets*, Wear, 488-489, 204136.
32. Perec, A., 2022, *Desirability Function Analysis (DFA) in Multiple Responses Optimization of Abrasive Water Jet Cutting Process*, Reports in Mechanical Engineering, 1(3), pp. 10-19.
33. Perec, A., Radomska-Zalas, A., Fajdek-Bieda, A., Pude, F., 2022, *Process optimization by applying the response surface methodology (RSM) to the abrasive suspension water jet cutting of phenolic composites*, Facta Universitatis-Series Mechanical Engineering, 21(4), pp. 575-589.
34. Hloch, S., Souček, K., Svobodová, J., Hromasová, M., Müller, M., 2022, *Subsurface microtunneling in ductile material caused by multiple droplet impingement at subsonic speeds*, Wear, 490–491, 204176.
35. Poloprudský, J., Chlupová, A., Šulák, I., Kruml, T., Hloch, S., 2021, *Surface and Subsurface Analysis of Stainless Steel and Titanium Alloys Exposed to Ultrasonic Pulsating Water Jet*, Materials, 14(18), 5212.